AGU PUBLICATIONS

JGR

Journal of Geophysical Research: Solid Earth

RESEARCH ARTICLE
10.1002/2016JB013645

Special Section:
Rock Physics of the Upper Crust

Experimental and numerical investigation of the temperature response to stress changes of rocks

Xiaoqiu Yang[1], Weiren Lin[2,3], Osamu Tadai[4], Xin Zeng[1], Chuanhai Yu[1], En-Chao Yeh[5], Haibing Li[6], and Huan Wang[6]

[1]CAS Key Laboratory of Ocean and Marginal Sea Geology, South China Sea Institute of Oceanology, Guangzhou, China, [2]Graduate School of Engineering, Kyoto University, Kyoto, Japan, [3]Kochi Institute for Core Sample Research, Japan Agency for Marine-Earth Science and Technology, Nankoku, Japan, [4]Marine Works Japan Ltd., Nankoku, Japan, [5]Department of Earth Sciences, National Taiwan Normal University, Taipei, Taiwan, [6]Institute of Geology, Chinese Academy of Geological Sciences, Beijing, China

Key Points:
- A new hydrostatic compression system was developed for measuring temperature response to stress changes of rocks under adiabatic conditions
- The temperature response to stress changes of 15 typical rock samples was investigated systematically
- A finite element model of heat conduction was built to confirm the measured results of temperature response to stress changes of rocks

Supporting Information:
- Supporting Information S1
- Table S1
- Movie S1
- Movie S2

Correspondence to:
X. Yang,
yxq2081@scsio.ac.cn

Citation:
Yang, X., W. Lin, O. Tadai, X. Zeng, C. Yu, E.-C. Yeh, H. Li, and H. Wang (2017), Experimental and numerical investigation of the temperature response to stress changes of rocks, *J. Geophys. Res. Solid Earth*, *122*, 5101–5117, doi:10.1002/2016JB013645.

Received 14 OCT 2016
Accepted 14 JUL 2017
Accepted article online 18 JUL 2017
Published online 31 JUL 2017

Abstract The temperature response to stress changes of rocks is key to understanding temperature anomalies in geoscience phenomena such as earthquakes. We developed a new hydrostatic compression system in which the rock specimen center can achieve adiabatic conditions during the first ~10 s following rapid loading or unloading and systematically measured several representative sedimentary, igneous, and metamorphic rocks sampled from two seismogenic zones (the Longmenshan Fault Zone in Sichuan and the Chelungpu Fault Zone (TCDP Hole-A) in Taiwan) and several quarries worldwide. We built a finite element model of heat conduction to confirm the measured results of temperature response to stress changes of rocks. The results show that (1) the adiabatic pressure derivative of the temperature (β) for most crustal rocks is ~1.5 mK/MPa to 6.2 mK/MPa, (2) the temperature response to stress of sedimentary rocks (~3.5–6.2 mK/MPa) is larger than that of igneous and metamorphic rocks (~2.5–3.2 mK/MPa), and (3) there is good linear correlation between β (in mK/MPa) and the bulk modulus K (in GPa): $\beta = (-0.068K + 5.69) \pm 0.4$, $R^2 = 0.85$. This empirical equation will be very useful for estimating the distribution of β in the crust, because K can be calculated when profiles of crustal density (ρ) and elastic wave velocities (V_p, V_s) are obtained from gravity surveys and seismic exploration.

Plain Language Summary The temperature responses of rocks to stress changes are key to understanding temperature anomalies in geoscience phenomena such as earthquakes. We developed a new hydrostatic compression system in which the rock specimen center can achieve adiabatic conditions during the first ~10 s following rapid loading or unloading and systematically measured several representative sedimentary, igneous, and metamorphic rocks sampled from two seismogenic zones and several quarries worldwide. We built a finite element model of heat conduction to confirm the measured results of temperature response to stress changes of rocks. The results show that (1) the adiabatic pressure derivative of the temperature for most crustal rocks is ~1.5 mK/MPa to 6.2 mK/MPa, (2) the temperature response to stress changes of sedimentary rocks is larger than that of igneous and metamorphic rocks, and (3) there is good linear correlation between the adiabatic pressure derivative of the temperature and the bulk modulus, which is therefore a useful empirical equation for estimating the distribution of the temperature response to stress changes in the crust, because the bulk modulus can be calculated much more easily.

1. Introduction

The thermal state of the crust can be influenced by a change in stress state. This change can be caused by various geological processes, e.g., mantle convection, plate motions, earth tides, volcanic eruptions, or earthquakes. In particular, when a huge earthquake occurs, the coseismic stress change occurs not only within the rupturing fault zone but also in the hanging/foot walls and even in a wider region [*Bouchon*, 1997; *Olsen et al.*, 1997]. Based on thermoelasticity theory, the temperature of rocks may change in association with the coseismic stress change that occurs at the same time as elastic deformation [*Boley and Weiner*, 1960; *Chen et al.*, 2016]. Seismic activity has been reported to alter surface and near-surface temperatures. For example, slow temperature changes prior to large earthquakes were first reported more than a century ago

[*Milne*, 1886]. Also, satellite thermal imaging data indicate long-term thermal fields associated with large linear structures and fault systems [*Carreno et al*., 2001] as well as short-term thermal anomalies prior to major earthquakes [*Ma and Shan*, 2000; *Tronin et al*., 2002; *Ouzounov and Freund*, 2004]. Additionally, systematic changes in groundwater temperature have been reported widely after earthquakes, such as the Tangshan earthquake in China (27 July 1976, M_w 7.8) [*Wang and Zhu*, 1984], the Chi-Chi earthquake in Taiwan (21 September 1999, M_w 7.6) [*Wang et al*., 2012; *Wang et al*., 2013], and the Tohoku earthquake in Japan (11 March 2011, M_w 9.0) [*Orihara et al*., 2014].

Recently, there have been numerous reports concerning temperature anomalies caused by seismic activity, examined from the ground surface and oceanic seafloor. For example, a basement rock temperature change was observed in Kangding before the Lushan earthquake in China (20 April 2013, M_w 7.0) [*Chen et al*., 2013, 2016]. Also, the seafloor water temperature increased (up to 0.1°C) in less than 10 h in the source region of the 2011 Tohoku earthquake [*Inazu et al*., 2014]. Furthermore, borehole temperature measurement results show that there were both positive and negative temperature anomalies that followed the 1999 Chi-Chi earthquake [*Kano et al*., 2006; *Tanaka et al*., 2006; *Tanaka et al*., 2007], the 2008 Wenchuan earthquake (12 May 2008, M_w 7.9) [*Li et al*., 2013; *Li et al*., 2015], and the 2011 Tohoku earthquake [*Fulton et al*., 2013]. The positive temperature anomaly has become well known because of the frictional heating that occurred during earthquake faulting [*Tanaka et al*., 2006; *Fulton et al*., 2013; *Li et al*., 2015]. However, the negative temperature anomaly still has not been noted and expressly addressed. In fact, not only frictional heating but also elastic deformation of rock can contribute to variations in temperature. However, the relationship between stress change or elastic deformation and temperature change has yet to receive much attention. Consequently, the temperature response properties associated with stress changes in rocks are key to improving understanding of temperature anomalies. Some theoretical and experimental studies have been conducted on the thermoelastic response of rocks and the thermodynamics of minerals [*Waldbaum*, 1971; *Richter and Simmons*, 1974; *Wong and Brace*, 1979; *McTigue*, 1986; *Wong et al*., 1987; *Wong et al*., 1988; *Stixrude and Lithgow-Bertelloni*, 2005; *Ma et al*., 2007; *Mosenfelder et al*., 2007; *Chen et al*., 2009; *Ma et al*., 2012; *Chen et al*., 2015]; however, it is still very difficult to carry out experiments under adiabatic conditions because there must be heat exchange when the loading/unloading system is open to the air.

Consequently, we developed a new hydrostatic compression system in which the center of the rock specimen can be identified by adiabatic conditions during the first several seconds (~10 s) following rapid loading or unloading and measured systematically using typical rocks sampled from the Longmenshan Fault Zone, the Taiwan Chelungpu-Fault Drilling Project (TCDP), Hole-A, and several quarries in the world.

2. Theoretical Background

The temperature of an elastic substance will change when it is compressed or stretched under adiabatic conditions. Based on classical thermoelastic theory, a convenient relationship between the temperature change (dT) and the sum of the principal stress changes (dS) can be expressed as

$$\mathrm{d}T = \frac{\alpha_l}{\rho c_\mathrm{p}} \cdot T_0 \cdot \mathrm{d}S, \tag{1}$$

where, T_0 is the thermodynamic temperature; ρc_p is the volumetric heat capacity at constant pressure; α_l is the coefficient of linear thermal expansion; $S = (\sigma_1 + \sigma_2 + \sigma_3)$ is the sum of the maximum, intermediate, and minimum principal stresses (σ_1, σ_2, and σ_3); and a positive value indicates compression in this study [*Boley and Weiner*, 1960; *Wong et al*., 1987; *Wong et al*., 1988]. In a hydrostatic compression system, the maximum, intermediate, and minimum principal stresses equate to the confining pressure P (i.e., hydrostatic pressure, and $\sigma_1 = \sigma_2 = \sigma_3 = P$). Therefore, the sum of the principal stresses equates to 3 times the confining pressure ($S = 3P$), and equation (1) can be rewritten as

$$\begin{cases} \mathrm{d}T = \beta \cdot \mathrm{d}P \\ \beta = \dfrac{\alpha_v}{\rho c_\mathrm{p}} \cdot T_0, \end{cases} \tag{2}$$

where, α_v is the coefficient of volumetric thermal expansion at thermodynamic temperature T_0, which is 3 times α_l (i.e., $\alpha_v = 3\alpha_l$). If $(\partial T/\partial P)_s$ is defined as the adiabatic pressure derivative of the temperature of the

rock at T_0, then we can measure $(\partial T/\partial P)_s$ by monitoring the temperature response of the rock to a confining pressure change under adiabatic conditions

$$\beta = (\partial T/\partial P)_S = \frac{\mathrm{d}T}{\mathrm{d}P}. \tag{3}$$

Chen et al. [2015] analyzed the principal stress-strain variation and temperature response in detail based on thermodynamics, elastic strain theory, and experiments on both ideal material and rock. Their results imply that temperature change is only related to the volume strain variation and that pure shear deformation does not contribute to temperature variation. Consequently, we can measure the adiabatic pressure derivative of the temperature ($\beta = \mathrm{d}T/\mathrm{d}P$) of a rock sample at T_0 directly by monitoring the temperature change of the rock sample ($\mathrm{d}T$) and the confining pressure change ($\mathrm{d}P$) that occur during a rapid loading or unloading process in the hydrostatic compression system.

3. Experimental Methods and Results

3.1. Rock Samples and Their Physical Properties

We prepared 15 cylindrical rock specimens with diameters (D) of 50.0 mm and lengths (L) of 50.0 mm. The samples included sandstone, siltstone, tuff, limestone, cataclasite, basalt, granite, and granodiorite. Nine samples were collected from the Longmenshan Fault Zone (Table S1 and Figure S1 in the supporting information) and two from the Taiwan Chelungpu Fault Drilling Project (TCDP), Hole-A (Figure S2). Several of these 11 rock samples were collected in or near seismic fracture zones that resulted from the Chi-Chi and Wenchuan earthquakes of 1999 and 2008 (Figures S1c and S2b). The other four rock samples are Rajasthan sandstone from India, Berea sandstone from the U.S., and Tage welded tuff and Karatsu basalt from Japan. All of the rock specimens were dried in an oven at 60°C for more than 5 days and then moved into a desiccator for cooling to room temperature while keeping dry. The basic physical properties of these rocks in a dry state were measured at room temperature (24–25°C) and atmospheric pressure (~0.1 MPa). The results are listed in Table 1. Grain densities (ρ_m), dry densities (ρ_{dry}), and porosities (ϕ) were measured based on the principle of buoyancy (the Archimedes principle) [*Franklin*, 1979]. Thermal conductivities (λ), thermal diffusivities (κ), and volumetric heat capacities (ρc) were measured at room temperature (24–25°C, with the exception of L28, L31, RJS, SS, and HS at 28–29°C and RJ and TG at ~20°C) and atmospheric pressure in a constant temperature box with the hot-disk method [*Gustafsson*, 1991; *ISO*, 2008; *Lin et al*., 2014]. Velocities of P waves (V_p) and S waves (V_s) were measured with 500 kHz and 100 kHz natural frequency oscillators, respectively. The elastic wave velocities were then used to calculate the dynamic Young's modulus (E), Poisson's ratios (ν), and bulk modulus (K) according to the methods for laboratory-based determination of pulse velocities and ultrasonic rock constants [*ASTM*, 1999]. The porosity and bulk modulus values of the 15 rocks range from 0.27% to 29.97% and 7.43 GPa to 52.06 GPa (except for the Tage welded tuff (TTF)), respectively, which corresponds to very large variations in the mechanical strength of these rocks. The bulk modulus decreases obviously with increasing porosity (Figure S3). Note that it was not easy to measure V_s of TTF due to its low mechanical strength and high porosity of ~29.97%. Therefore, we have no data for the Young's modulus (E), Poisson's ratio (ν), or bulk modulus (K) of TTF.

3.2. Measurement System

To load and unload rapidly, we developed a new hydrostatic compression system with two pressure vessels and a servo-controlled pump that provides pressure of up to 130 MPa at room temperature (~22–24°C) (Figure 1). Both pressure vessels are filled with silicone oil as the pressure medium. To avoid oil permeating into the pores of the rock sample, there are two dielectric silicone and rubber end pieces, each 50 mm in height, at the top and bottom of the rock specimen. The silicone end piece includes two parts, each 25 mm thick (Figures 1 and 2a). One is hard silicone. The other is soft silicone, which is made of two original silicone components produced by Shin-Etsu Chemical Co., Ltd (Figure S4). Figure S5 shows the assembly process in detail. And there is the detailed description about the sample assembly in the supporting information. Between the rock specimen and the silicone/rubber end pieces, there are two pieces of 5 mm thick hard plastic (Figures 2a and 2b). There is a hole with a diameter of 2.8 mm in the center of the top hard plastic piece (Figure S5c).

Journal of Geophysical Research: Solid Earth

10.1002/2016JB013645

Table 1. Physical Properties of Dry Rock Samples and Auxiliary Materials[a]

No.	Sample ID	Lithology or Material	ρ_m (g/m^3)	ρ_{dry} (g/m^3)	ϕ (%)	V_p (m/s)	V_s (m/s)	E (GPa)	ν	K (GPa)	λ (W/(m K))	κ (mm^2/s)	(ρc) (MJ/(m^3·K))	$\bar{\beta}$ (mK/MPa)	T_0 (°C)	Note
1	L17	Sandstone	2.752	2.634	4.29	3553	1621	18.95	0.37	24.03	2.03	1.16	1.750	4.03	~23	From LMS Fault Zone
2	L20	Sandstone	2.746	2.701	1.67	3535	1987	27.07	0.27	19.54	2.55	1.58	1.614	4.10	~23	From LMS Fault Zone
3	L23	Sandstone	2.774	2.720	1.93	3710	2227	32.87	0.22	19.46	2.59	1.39	1.869	4.35	~23	From LMS Fault Zone
4	L28	Siltstone	2.763	2.487	9.99	3744	1725	20.21	0.37	24.99	1.37	1.08	1.261	3.66	~23	From LMS Fault Zone
5	L31	Lithic sandstone	2.725	2.694	1.16	4707	2679	48.74	0.26	33.90	3.62	1.68	2.158	3.58	~23	From LMS Fault Zone
6	C01	Siltstone	2.711	2.413	11.01	3548	1995	24.37	0.27	17.57	2.22	1.12	1.991	4.28	~23	From TCDP Hole-A, Chelungpu Fault. The depth is 1105.43–1105.73 m
7	C02	Sandstone with bioturbation	2.687	2.358	12.22	3045	1716	17.61	0.27	12.60	2.51	1.14	2.192	4.81	~23	From TCDP Hole-A, Chelungpu Fault. The depth is 484.75–484.93 m
8	RJS	Sandstone	2.605	2.340	10.18	3233	1987	22.10	0.20	12.14	3.27	1.88	1.737	4.71	~23	From Rajasthan, India
9	BRS	Sandstone	2.623	2.098	20.03	2321	1175	7.69	0.33	7.43	2.35	1.54	1.528	5.86	~23	From Berea, Ohio, USA
10	L27	Limestone	2.720	2.713	0.27	5320	2812	56.04	0.31	48.20	3.14	1.37	2.287	1.53	~23	From LMS Fault Zone
11	TTF[b]	Welded tuff	2.429	1.701	29.97	1526	-	-	-	-	0.90	0.61	1.471	6.15	~22	From Tage, Tochigi Prefecture, Japan
12	L25	Cataclasite	2.730	2.697	1.22	3657	2009	27.94	0.28	21.55	3.24	1.44	2.245	4.24	~22	From LMS Fault Zone
13	L35	Granite	2.648	2.635	0.51	5050	2699	49.89	0.30	41.62	3.19	1.36	2.352	3.16	~23	From LMS Fault Zone
14	L24	Granodiorite	2.713	2.696	0.63	5390	2703	52.46	0.33	52.06	2.65	1.31	2.026	2.92	~22	From LMS Fault Zone
15	KBT	Basalt	2.939	2.717	7.56	4892	2438	43.12	0.33	43.48	1.49	0.76	1.967	2.69	~23	From Karatsu, Saga Prefecture, Japan
16	HP	Hard plastic	1.184	-	-	-	-	-	-	-	0.20	0.12	1.740	38.35	~23	Auxiliary material
17	HR	Hard rubber	1.554	-	-	-	-	-	-	-	0.48	0.26	1.819	57.95	~23	Auxiliary material
18	HS	Hard silicone	1.139	-	-	-	-	-	-	-	0.24	0.15	1.601	127.54	~22	Auxiliary material
19	SS	Soft silicone	1.236	-	-	-	-	-	-	-	0.29	0.18	1.617	132.31	~23	Auxiliary material
20	RJ	Rubber jacket	0.929	-	-	-	-	-	-	-	0.16	0.09	1.6624	97.48	~22	Auxiliary material
21	TG[c]	Thermal grease	-	-	-	-	-	-	-	-	0.51	0.37	1.3918	-	-	Auxiliary material
22	Oil[d]	Silicone oil	-	-	-	-	-	-	-	-	-	-	-	138.74	~23	Auxiliary material
23	WT	Tap water	-	-	-	-	-	-	-	-	-	-	-	17.67	~21	

[a] ρ_m, ρ_{dry}, and ϕ are the grain density, dry density, and porosity, respectively. V_p, V_s, E, ν, and K are the velocities of P and S waves, Young's modulus, Poisson's ratio, and bulk modulus, respectively. λ, κ, and ρc are thermal conductivity, thermal diffusivity, and volumetric heat capacity, respectively. The thermal properties were measured at 24–25°C (except for L28, L31, RJS, SS, and HS at 28–29°C and RJ and TG at ~20°C) at atmospheric pressure in a constant temperature box. $\bar{\beta}$ is the measurement result of the adiabatic pressure derivative of the temperature $(\partial T/\partial P)_S$ of the rock sample at room temperature T_0, which is listed in Table S2 in detail. LMS, Longmenshan.

[b] We have no data concerning E, ν, and K for the Tage welded tuff (TTF) since it was not easy to measure V_s of Tage welded tuff (TTF) due to its low mechanical strength and high porosity of about 29.97%.

[c] This is a kind of thermally conductive silicone grease (Tianmu) produced by Hongda Rubber Industry Co., Ltd. Its thermal properties were measured with the hot-disk method, too, in the Key Lab of Shale Oil and Gas Geological Survey, Chinese Academy of Geological Sciences.

[d] This is a kind of dimethyl organic silicone oil (KF-96-50CS) produced by Shin-Etsu Chemical Co., Ltd.

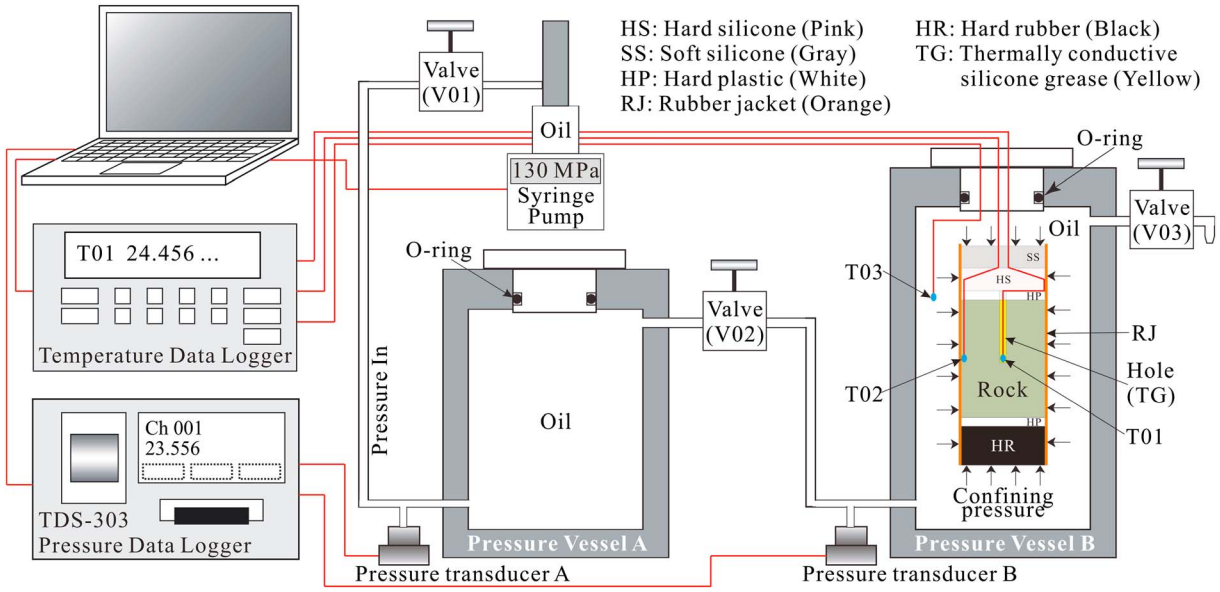

Figure 1. Schematic diagram of the new hydrostatic compression system developed in this study for measurement of the adiabatic pressure derivative of the temperature (β). The system consists of two pressure vessels with a servo-controlled pump that provides pressure up to 130 MPa. The sample assembly is placed in Pressure Vessel B. The volumes of Vessels A and B, the syringe pump, and sample assembly are about 88 cm^3, 1257 cm^3, 65 cm^3, and 340 cm^3, respectively. Three temperature sensors (T01 in sample center, T02 on sample surface, and T03 in oil around the rock specimen in the Pressure Vessel B) were deployed for monitoring temperature changes during rapid loading/unloading processes, along with a temperature data logger and a confining pressure data logger.

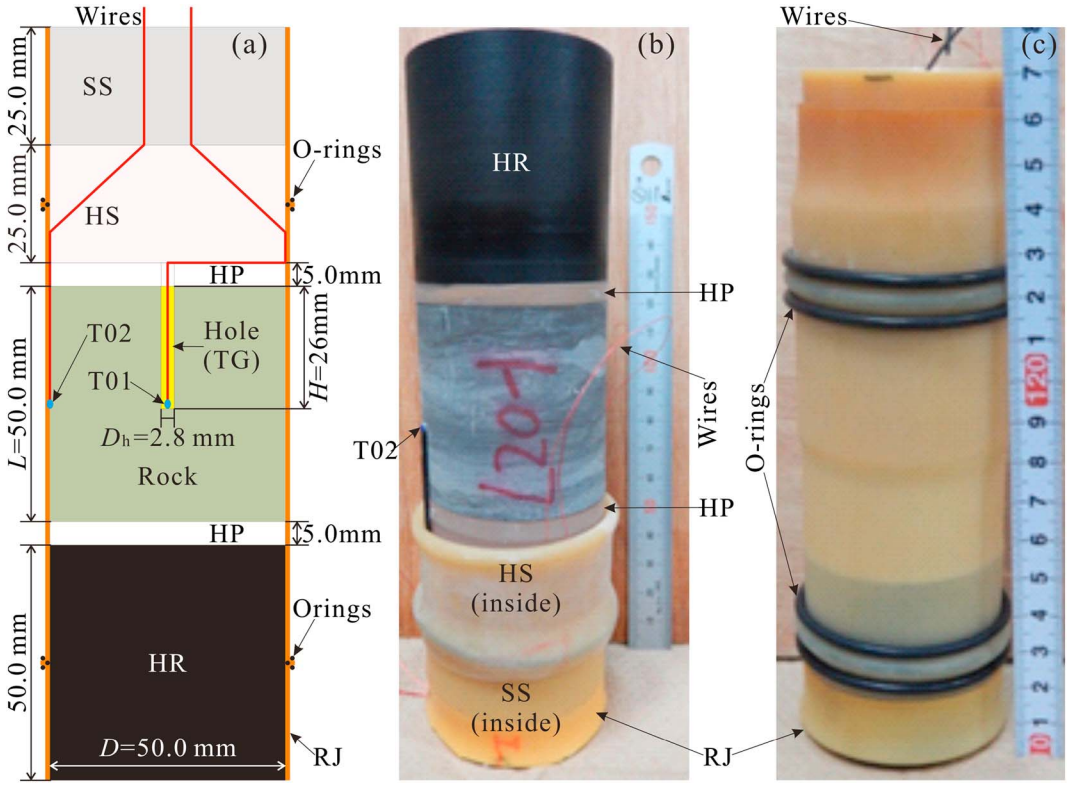

Figure 2. (a) Schematic diagram and pictures of rock specimen assembly (b) before and (c) after being enveloped with rubber jacket and O-rings. HS is hard silicone (pink), SS is soft silicone (gray), HP is hard plastic (white), RJ is rubber jacket (orange), HR is hard rubber (black), and TG is thermally conductive silicone grease (yellow). The size of temperature sensors is 1.95 mm × 1.25 mm × 0.93 mm, and the diameter of wires is 0.2 mm.

All of the silicone, rubber, and plastic pieces are 50 mm in diameter, like the rock specimen (Figure 2a). We enveloped them together with a rubber jacket and three O-rings on each end piece. One O-ring is between the hard silicone/rubber end piece and the rubber jacket. Two are around the outside of the rubber jacket (Figures 2a and 2c). After measuring the primary physical properties, we drilled a hole that was 2.8 mm in diameter (D_h) and 26.0 mm in depth (H) in the center of each rock specimen (Figures 1 and 2a). Then, we installed temperature sensors (PT1000 M213 Class-B, one kind of platinum resistance temperature detector produced by the Heraeus Sensor Technology GmbH, Kleinostheim, Germany) through the silicone end piece and the top hard plastic piece in the center (T01) and on the surface (T02) of the sample in addition to a temperature sensor in the oil (T03) (Figures 1, 2a, and 2b and S5c). The three temperature sensors were connected to the temperature data logger, which we designed based on a bridge reversal excitation circuit with a high temperature resolution of ~1.0 mK at room temperature [*Qin et al*., 2013]. The center hole of the specimen was filled with thermally conductive silicone grease (yellow area in Figures 1 and 2a), which is a type of paste material similar to toothpaste (Figure S6) and is very effective for sensitive response of the sensor T01 to the temperature change in the rock sample center. Thus, during the rapid loading and unloading processes, we can monitor the confining pressure (oil pressure, P) and temperature changes of the rock specimen and oil with the pressure data logger (TDS-303, Tokyo Sokki Kenkyujo Co. Ltd, Tokyo, Japan) and the temperature data logger with a data sampling interval of 1 s.

3.3. Experimental Procedure

After the dry rock specimen was cooled to room temperature in a desiccator, the experiment consisted of four main steps. (1) We placed the sample assembly in Vessel B and closed valves V02 and V03 while keeping valve V01 open (Figure 1). (2) We increased the confining pressure in Vessel A to a predetermined high pressure (e.g., 125 MPa) using the servo-controlled pump and kept it constant at room temperature for at least 4 h for the system to achieve temperature equilibrium, as much as that was possible. During this period, the confining pressure in Vessel B was kept at a lower pressure. (3) We rapidly loaded the rock specimen by manually opening valve V02. The confining pressure in Vessels A and B should be the same after opening valve V02, and it was kept constant for more than 4 h to enable the system temperature to reach equilibrium again. (4) We then closed valve V02 and opened valve V03 to instantaneously unload the confining pressure in Vessel B to atmospheric pressure. For each rock specimen, a set of tests was carried out with a range of confining pressure changes. The key experimental records and results are listed in Table S2. The maximum confining pressure in Vessel B was set to 50 MPa, which is much lower than the strength of the rocks. Therefore, there is no influence of stress loading history on the temperature response during multiple tests for the same rock specimen.

Taking the fifth loading and unloading test for Rajasthan sandstone (RJS-05) as an example, the system temperature tended to equilibrium at around 23°C (Table S2), after waiting for more than 4 h following the installation of the specimen in Vessel B. During the temperature equilibrium period, the confining pressures in Vessels A and B were kept at 125 MPa and 1.7 MPa, respectively. At 13:57:51 (equivalent to t = 0 s in Figure 3a1), valve V02 was rapidly opened manually. The confining pressure in Vessel A rapidly reduced to 13.61 MPa from 125 MPa within 1–2 s. Coincident with this, the confining pressure in Vessel B rapidly increased from 1.7 MPa to 13.61 MPa (Figures 3a1 and 3a2). During this rapid loading process, we observed a rapid rise in temperature of the Rajasthan sandstone (T01 in center and T02 on surface) and oil (T03) (Figures 3a1 and 3a2), followed by a gradual decrease. About 4 h later, the whole system had almost achieved temperature equilibrium (~23°C) once again (Figure 3a1). Finally, we opened valve V03 manually at 18:03:00 (t = 14710 s in Figure 3a1 and t = 0 s in Figure 3a3). The confining pressure then dropped almost instantaneously to atmospheric pressure (~0.1 MPa) from 13.36 MPa within 1–2 s (Figures 3a1 and 3a3). The temperature of the rock specimen and oil dropped rapidly at the same time. Finally, the system temperature slowly reverted to room temperature. During tests L28-08 and TTF-01, similar temperature responses were recorded by the same procedure and operation (Figures 3b1–3b3 and 3c1–3c3). These results indicate that the hydrostatic compression system can be successfully used to rapidly load and unload within 1–2 s.

3.4. Experimental Data Analysis

In this section, the relationship between the confining pressure change (dP) in Vessel B and temperature change in the rock specimens (dT) during the loading/unloading process is analyzed in detail. From Figure 3, it is not easy to understand the temperature change of the rock sample (dT01) during the

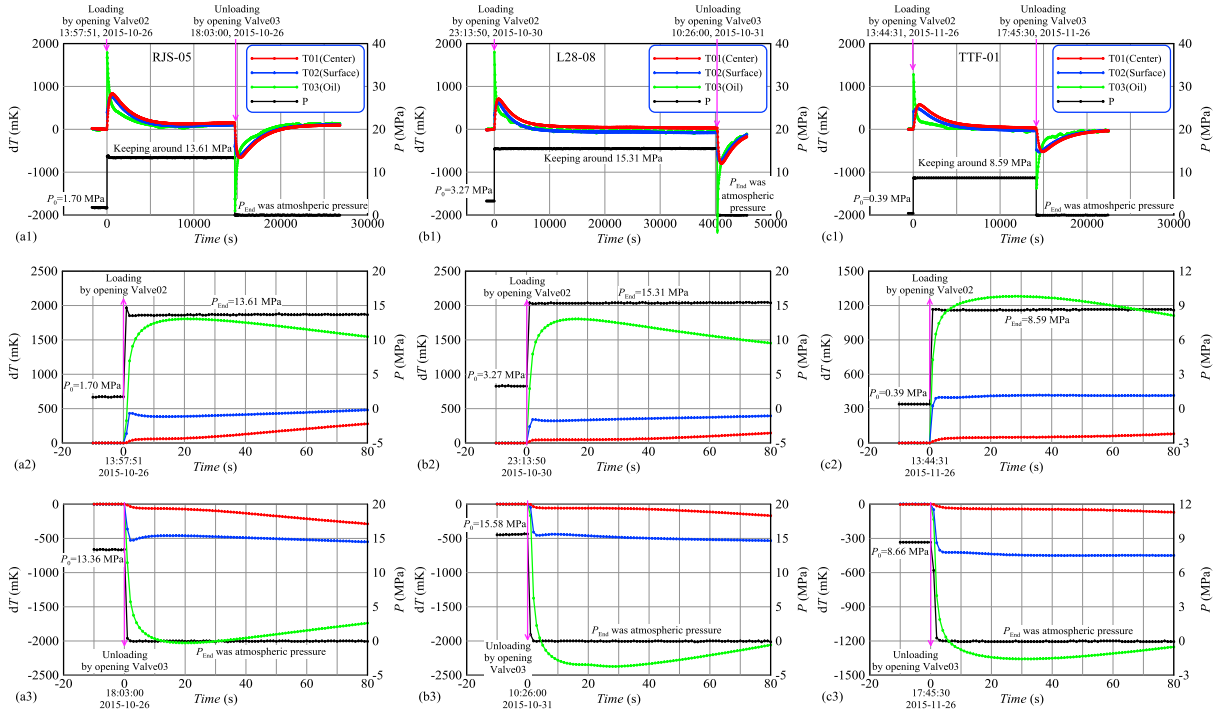

Figure 3. Changes of temperature (d*T*) and confining pressure (d*P*) in Vessel B during (a1, b1, c1) the loading and unloading processes for tests RJS-05, L28-08, and TTF-01, (a2, b2, c2) only the loading process, and (a3, b3, c3) only the unloading process, respectively. The rock specimens in tests RJS-05, L28-08, and TTF-01 are sandstone, siltstone, and welded tuff from Rajasthan, India; Longmenshan Fault Zone, China; and Tage, Japan; respectively. T01 is in the sample center, T02 is on the surface of sample, and T03 is in oil. The background temperature (around 23°C, see in Table S2) was removed (similarly hereinafter). Thus, only temperature changes are seen here. In tests RJS-05, L28-08, and TTF-01, the point of rapid loading/unloading are set to be the initial times (i.e., t = 0, similarly hereinafter).

loading/unloading process because the temperature change of oil (d*T*03) was much larger during the same period. However, d*T*01 is the true rock sample temperature change that we want to know in detail. Therefore, here we only show the changes of confining pressure in Vessel B and the center temperature of rock specimens in tests RJS-05 (Figures 4a1 and 4a2), L28-08 (Figures 4b1 and 4b2), and TTF-01 (Figures 4c1 and 4c2) during the loading/unloading process, respectively.

Figure 4 illustrates that there are steps in the center temperature change from t = 7 s to t = 14 s in test RJS-05 (Figures 4a1 and 4a2), t = 10 s to t = 20 s in test L28-08 (Figures 4b1 and 4b2), and t = 16 s to t = 30 s in test TTF-01 (Figures 4c1 and 4c2) after rapid manual opening of valves V02 or V03, respectively (this is the basis for

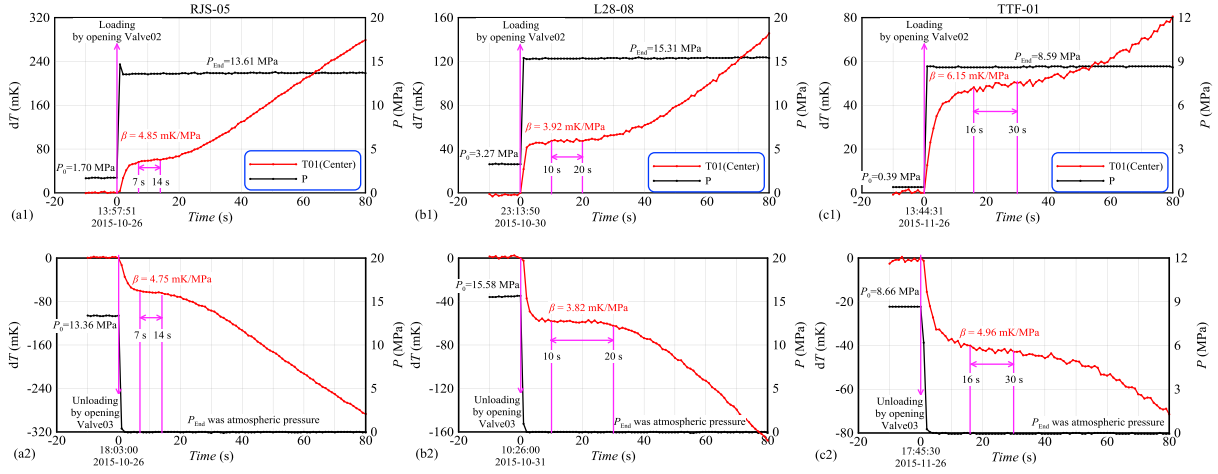

Figure 4. Changes of confining pressure (d*P*) in Vessel B and temperature (d*T*) in the center of rock specimens during rapid loading and unloading processes in tests (a1, a2) RJS-05, (b1, b2) L28-08, and (c1, c2) TTF-01, respectively.

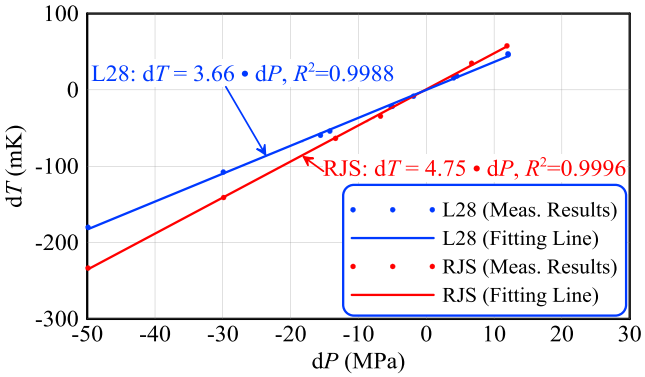

Figure 5. Temperature changes (d*T*) of rock samples L28 and RJS for different confining pressure changes (d*P*) and the linear fitting results.

selecting the steps of each test in section 4.2, Numerical Predictions and Comparison With Experimental Results). In theory, the center temperature of the rock sample (d*T*01) should change instantaneously after opening the valve. However, the center hole was full of thermally conductive silicone grease, which needs an input/output of energy before its temperature rises to the rock sample temperature during rapid loading/unloading process. Thus, after opening valve V02 or V03, the actual measured temperature changed gradually until the rock sample and silicone grease achieved temperature equilibrium. This process lasted about 7 s for Rajasthan sandstone, 10 s for L28 siltstone, and 16 s for Tage welded tuff (Figure 4). The temperature steps reveal that the center temperature of the rock specimens was not disturbed by the large temperature change in the oil but rather was only affected by changes in the hydrostatic pressure during the first 14 s, 20 s, and 30 s in tests RJS-05, L28-08, and TTF-01, respectively. The temperature data also indicate that the change was an adiabatic compression/decompression process during the first 14 s, 20 s, and 30 s in tests RJS-05, L28-08, and TTF-01, respectively. Consequently, accurate adiabatic pressure derivatives of the temperature of rock specimens RJS (β_{RJS}), L28 (β_{L28}), and TTF (β_{TTF}) can be obtained easily from the center temperature responses of the rock specimens due to the confining pressure changes during the first 7 s to14 s, 10 s to 20 s, and 16 s to 30 s after opening the valves. The results show that β_{RJS} are about 4.85 mK/MPa and 4.75 mK/MPa, β_{L28} are about 3.92 mK/MPa and 3.82 mK/MPa, and β_{TTF} are about 6.15 mK/MPa and 4.96 mK/MPa during the rapid loading/unloading process in tests RJS-05, L28-08, and TTF-01, respectively (Figure 4). Values for β_{RJS}, β_{L28}, and β_{TTF} are slightly higher during the loading process, because the pressure changes were a little greater during the unloading process than that during the loading process in the three tests, and β decreases as the confining pressure change increases for most of the rocks. This will be discussed in detail in section 5.2, β Dependence on Levels of Stress Changes.

For each rock specimen, a set of tests was carried out at different confining pressure changes (Table S2). As an example, Figure 5 shows the temperature changes (d*T*) in rock samples L28 and RJS for different confining pressure changes (d*P*) and linear fitting results. Thus, $\overline{\beta}_{L28}$ and $\overline{\beta}_{RJS}$ are determined to be 3.66 mK/MPa and 4.75 mK/MPa at ~23°C, respectively.

3.5. Experimental Results

In this study, we carried out a set of tests for each dry rock specimen with various confining pressure changes using experimental procedures as outlined above. Based on step changes observed in the rock sample center during rapid loading/unloading process, we obtained the adiabatic pressure derivatives of the temperature ($\overline{\beta}$) for 15 rock samples (Table 1). We also measured tap water (WT) and six kinds of auxiliary materials: hard plastic (HP), hard rubber (HR), hard silicone (HS), soft silicone (SS), rubber jacket (RJ), and silicone oil (Oil), using the same methods. The measurement results show that β for most crustal rocks is about 1.5 mK/MPa to 6.2 mK/MPa, and the temperature response of the sedimentary rocks (~3.5–6.2 mK/MPa) is larger than that of igneous and metamorphic rocks (~2.5–3.2 mK/MPa) (Table 1). Key experimental records and results are listed in Table S2.

4. Numerical Analysis

A finite element model of heat conduction was first built to analyze the temperature change in the center of the rock specimens. We then solved for the temperature distribution in the specimens during the loading events, taking tests RJS-05, L28-08, and TTF-01 as examples. Finally, by comparing numerical predictions with experimental results, we determined reliable β values for tests RJS-05, L28-08, and TTF-01 during the loading process.

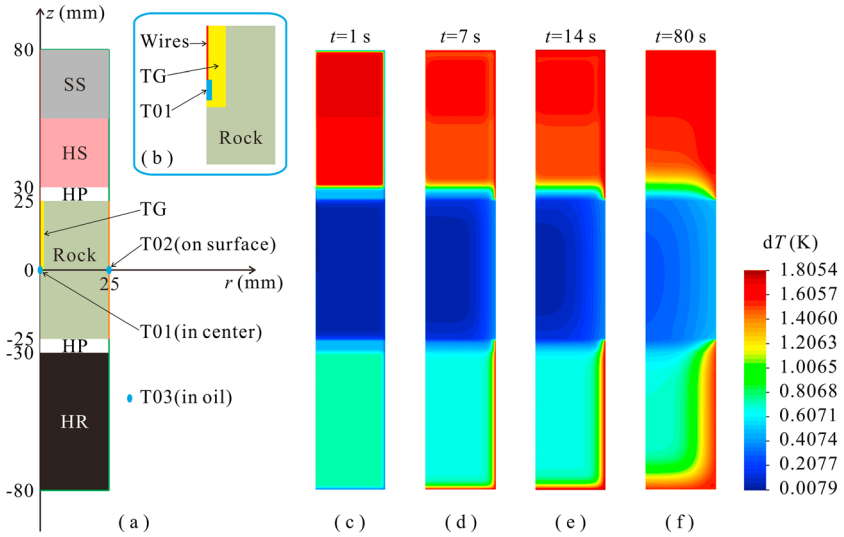

Figure 6. (a) Schematic diagram of heat conduction finite element model in a 2d*rz* system, (b) the local structure around the temperature sensor T01 in the center hole, and the temperature profiles at (c) 1 s, (d) 7 s, (e) 14 s, and (f) 80 s after rapid loading in test RJS-05, respectively. The size of temperature sensors is 1.95 mm × 1.25 mm × 0.93 mm, and the diameter of each wire is 0.2 mm. So the equivalent radii of the temperature sensor T01 and the four wires are 0.4 mm and 0.14 mm in the finite element model, respectively.

4.1. Numerical Method

The experimental results presented previously show that changes in the center temperature of rock specimens were only due to hydrostatic pressure change during the first 14 s, 20 s, and 30 s following loading/unloading in tests RJS-05, L28-08, and TTF-01, respectively (Figure 4). To have a clearer understanding of temperature changes, a heat conduction finite element model framed in a two-dimensional cylindrical coordinate system (2d*rz*) was built to obtain temperatures (T) at radii (r) and depths (z) from the rock sample center along the radial and axial directions, respectively. The heat conduction equation in the 2d*rz* system is expressed as

$$(\rho c)\frac{\partial T}{\partial t} = \lambda\left(\frac{1}{r}\frac{\partial T}{\partial r} + \frac{\partial^2 T}{\partial r^2} + \frac{\partial^2 T}{\partial z^2}\right) + A, \tag{4}$$

$$A = \beta(\rho c)\frac{\partial P}{\partial t}, \tag{5}$$

with the initial condition

$$T(r, z, 0) = 0, r \le 25\,\text{mm}, |z| \le 80\,\text{mm} \tag{6}$$

and boundary conditions given by experimental records from temperature sensors T02 and T03,

$$T(r,z,t) = \begin{cases} T02(t), r = 25\,\text{mm} |z| \le 25\,\text{mm} \\ T03(t), \begin{cases} r = 25\,\text{mm}, \;\; 25\,\text{mm} < |z| < 80\,\text{mm}, \\ |z| = 80\,\text{mm} \end{cases} \end{cases} \tag{7}$$

where λ is the thermal conductivity, ρc is the volumetric heat capacity, β is the adiabatic pressure derivative of the temperature, and A is the "heat source" term driven by confining pressure change. The measurements for λ, ρc, and β of all rocks and auxiliary materials are listed in Table 1.

Figures 6a and 6b show a finite element geometric model of the rock sample assembly used in this study and the local structure around the temperature sensor T01. In this model, only half of the rock specimen section is shown because all rock specimens are axially symmetrical along the center axis. The rock specimen (gray-green) is in the center, and the end pieces of hard/soft silicone (pink/gray) and hard rubber (black) are at the top and bottom, respectively. Between the rock specimen and hard silicone/hard rubber, there

Table 2. Thermal Properties of the Hard Ceramic and Constantan

Sample ID	Material	T_0 (°C)	λ (W/(m K))	(ρc_p) (MJ/(m^3 K))	κ (mm^2/s)	$\alpha_v \times 10^{-6}$ (1/K)	β^a (mK/MPa)	References
HC	Hard ceramic	25	1.40 (1.20–1.62)	2.295 (2.268–2.322)	0.61 (0.53–0.71)	21.0 (19.5–22.5)	2.73 (2.56–2.89)	*Liu* [1981]
CNA	Constantan (60Cu-40Ni)	25	22.20	3.657	6.07	56.4	4.60	*Lide* [2010]

[a] β of hard ceramic and constantan were calculated values using equation (2).

are two pieces of hard plastic (white). The temperature sensors (T01, T02, and T03) and the sizes of the rock specimen and pieces of hard silicone, plastic, and rubber are marked. This model was meshed to 6435 quadrilateral elements. In this model, the spatial resolution is within 1.0 mm (i.e., dr < 1.0 mm and dz < 1.0 mm), especially in the local area around the axial hole. The initial temperature of both the rock specimen and hard silicone was set to be 0°C, because the experimental system almost tended to temperature equilibrium before loading and unloading (equation (6)). The temperature boundaries of rock specimens (orange line in Figure 6a) and silicone, plastic, and rubber pieces (green lines in Figure 6a) were based on measurements on the rock surface (T02) and in oil (T03) which are shown in Figure 3 (equation (7)). In this model, the thermal conductivities (λ) and the volumetric heat capacities (ρc) of rock samples and silicone, plastic, rubber, and thermally conductive silicone grease were measured at room temperature and atmospheric pressure with the hot-disk method, too [*Gustafsson*, 1991; *ISO*, 2008; *Lin et al*., 2014] (Table 1). The temperature sensors are PT1000 platinum resistance detectors in which the major component is hard ceramic (HC) with very thin platinum film. The material of the electrical wires is constantan which is a kind of copper nickel alloy (CNA: 60Cu-40Ni). The thermal properties of the hard ceramic and the constantan are listed in Table 2.

The "heat sources" (A) of rock samples and auxiliary materials can be calculated by equation (5) because β had been measured (Table 1), and the confining pressure change rate ($\partial P/\partial t$) can be obtained from the loading/unloading test records. There is a hole in the center of the hard plastic between the hard silicone piece and the rock sample. This hole was not filled with anything, expect for the four electric wires (Figures 1, 2a, and S5c). The diameter of the hole is 2.8 mm. The diameter of each wire is only 0.2 mm. Therefore, there is space for the thermally conductive silicone grease to freely deform if the volume change of the rock sample is not too large under confining pressure. This means that there is no stress change in the hole during confining pressure cycling. If the conductive grease experiences compression/decompression, the temperature in the hole center should increase/decrease immediately after loading/unloading. All experimental results show that the temperature in the hole center (T01) always increased/decreased gradually during the first several seconds after rapid loading/unloading (Figure 4). Therefore, the "heat source" term in the hole can be set to be 0 (i.e., $A = 0$) because the stress change rate was 0 ($\partial P/\partial t = 0$).

4.2. Numerical Predictions and Comparison With Experimental Results

Based on the finite element model described previously, with its initial and boundary conditions, we solved for the temperature distribution during the loading processes in tests RJS-05, L28-08, and TTF-01. The temperature profiles at 1 s, 7 s, 14 s, and 80 s after the instantaneous loading process in test RJS-05 are illustrated in Figures 6c–6f, respectively. Comparisons between the measured and predicted changes in the center temperature during the first 80 s in the three tests are shown in Figures 7a1, 7b1, and 7c1. The measured T01(Meas) and modeled T01(Mod) temperature curves reveal almost the same temperature changes during loading processes in each test. Figures 7a2, 7b2, and 7c2 show the change rate of temperature (dT01/dt) in the hole center. The trends for the measured, dT01/dt(Meas), and modeled, dT01/dt(Mod), change rates of temperature are almost the same, too, although the dT01/dt(Meas) fluctuates more widely than dT01/dt(Mod) because the resolution of the PT1000 temperature sensors is about 1.0 mK at room temperature [*Qin et al*., 2013]. This means that both the measured and predicted results were accurate and reliable.

It is worth noting that the experimental and modeled results show that the temperature in the hole center (T01) always increased gradually during the first several seconds after instantaneous loading, then kept nearly constant for a short period, before finally rising again in all tests (Figure 7). Thus, there are the very obvious steps in the center temperature change. During the steps, the change rates of temperature

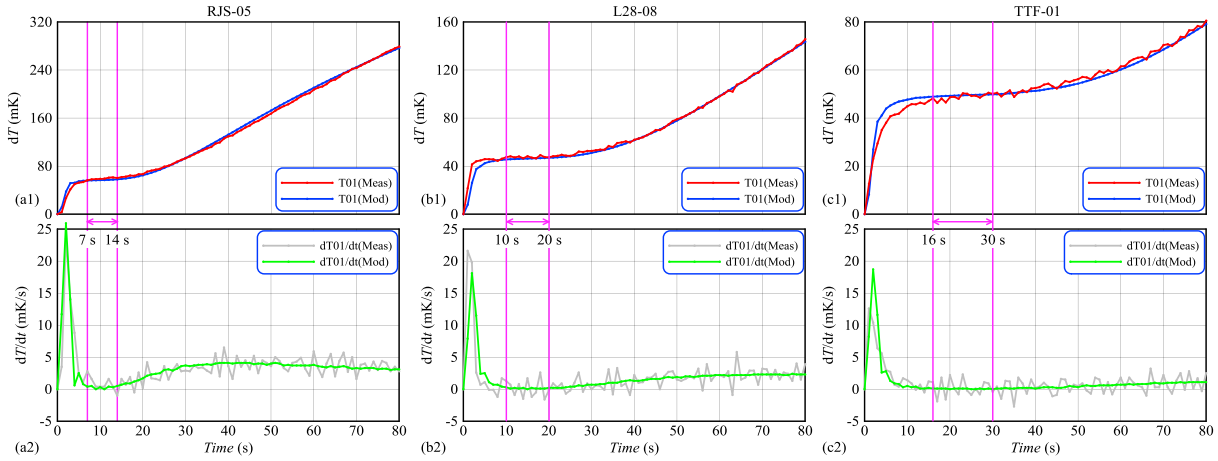

Figure 7. The experimental and numerical results of the temperature change in the hole center of the RJS, L28, and TTF specimens during loading processes in tests RJS-05, L28-08, and TTF-01, respectively. The *T*01(Meas) and *T*01(Mod) are measured (red lines) and modeled (blue lines) temperature curves. The d*T*01/d*t*(Meas) and d*T*01/d*t*(Meas), are the measured (gray lines) and modeled (green lines) change rates of temperature, respectively.

(d*T*/d*t*) are almost 0, especially in the curves for d*T*01/d*t*(Mod) (green lines in Figures 7a2, 7b2, and 7c2). The change rates of temperature are up to ~15–20 mK/s before the steps and increase slowly after the steps. This means that the thermally conductive silicone grease absorbs heat from the rock sample until the local area around the hole achieves temperature equilibrium. After keeping a constant temperature for several seconds, the center temperature is affected by heat conduction from oil. Movies S01 and S02 provide very clear images to understand the inner temperature evolution of the whole rock specimen during the loading/unloading process.

The numerical simulation results provide not only a strong evidence that all the measurements made by the new hydrostatic compression system developed for this study are reliable but also a basis to determine the range of the steps which represent an adiabatic condition. In addition, the experimental and modeled results indicate that temperature step periods during the loading/unloading process are dependent on the thermal diffusivities (κ) of the rock samples. For example, the periods of the temperature step in tests RJS-05, L28-08, and TTF-01 are 7–14 s, 10–20 s, and 16–30 s, respectively, because the κ values of RJS, L28, and TTF are 1.88 mm^2/s, 1.08 mm^2/s, and 0.61 mm^2/s (Table 1), respectively. This indicates that the temperature step periods in the rock sample center will increase as κ decreases.

Consequently, it is easy to calculate β accurately for other rock samples based on the steps in the center temperature change during the loading/unloading processes. For example, β values for RJS (β_{RJS}), L28 (β_{L28}), and TTF (β_{TTF}) were found to be 4.85 mK/MPa, 3.92 mK/MPa, and 6.15 mK/MPa during the loading processes in tests RJS-05, L28-08, and TTF-01, respectively. These results can be confirmed by comparing the center temperature changes in numerical predictions made with the finite element model with the experimental results.

5. Discussion

5.1. β of Granite and Water

Cooper and Simmons [1977] measured the coefficients of volumetric thermal expansion (α_v) of several granite samples from different regions with the equipment and techniques described by *Richter and Simmons* [1974]. Their results for granite ranged from 1.99×10^{-5}/K to 2.51×10^{-5}/K at 25°C. The densities of their granite samples are about 2.60 g/cm to 2.65 g/cm. Our measurement for dry granite (L35) from the Longmenshan Fault Zone is about 2.635 g/cm (Table 1), which is close to the results of *Cooper and Simmons* [1977]. If we assume that the coefficient of volumetric thermal expansion of L35 is within the range of the results of *Cooper and Simmons* [1977], and the volumetric heat capacity at constant ρc_p is not greatly affected by pressure, we can estimate the β value of L35 granite (β_{L35}) by equation (2), using the measured volumetric heat capacity of L35 from this study (ρc = 2.352 MJ/(m^3 K), Table 1). The calculated β_{L35} ranges from 2.52 mK/MPa to 3.18 mK/MPa (Table 3). The measured β_{L35} ranges between 3.14 mK/MPa and 3.37 mK/MPa, which is close to the calculated range (Table S2).

Table 3. Comparison Between Calculated and Measured β for Granite and Water

Sample ID	Lithology or Material	T_0 (°C)	$\alpha_v \times 10^{-6}$ (1/K)	(ρc_p) (MJ/(m^3 K))	β (mK/MPa) Calculated	β (mK/MPa) Measured	References
L35[a]	Granite	25	19.9-25.1	2.352	2.52–3.18	3.14–3.37	*Cooper and Simmons* [1977]
WT[b]	Tap water	21	227.72	4.173	16.10	17.67	TEOS-10

[a] ρc_p and β of granite (L35) were measured at about 24°C and 23°C, respectively, in this study (Table 1).
[b] ρc_p of tap water was calculated at 21°C and atmospheric pressure (~0.1 MPa) when the salinity of tap water is assumed to be nearly 0 according to TEOS-10 (the official source of information about the Thermodynamic Equation of Seawater, 2010, http://www.Marine.Csiro.Au/~jackett/TEOS-10).

In addition, as the salinity of tap water is assumed to be near 0, we calculated the β of tap water to be about 16.1 mK/MPa at 21°C and atmospheric pressure, because the density (ρ), specific heat at constant pressure (c_p), and coefficient of volumetric thermal expansion (α_v) of tap water can be estimated under any conditions by TEOS-10 (the official source for information about the Thermodynamic Equation of Seawater, 2010, http://www.marine.csiro.au/~jackett/TEOS-10).

In comparing the calculated β of granite (L35) and tap water (WT) with the results of this study, the measurements are found to be consistent with estimated values. Consequently, this provides another strong evidence that the measurement results from the hydrostatic compression system developed in this study are reliable.

5.2. β Dependence on Levels of Stress Changes

For each rock specimen, a set of tests was carried out with different confining pressure changes (Table S2). Because the shear stress in the hydrostatically pressured specimen was 0, and the hydrostatic pressure values in the tests were much lower than the strength of the rock, it can be assumed that there was no damage caused by the pressure cycles; i.e., effects caused by hydrostatic pressure history can be ignored. The results indicate that β decreases with an increase in the change of confining pressure ($|dP|$) for most rocks and silicone oil when $|dP|$ is less than 50 MPa (Figure 8 and Table S2). This is particularly important for estimating the temperature change with the coseismic stress drop, which was found to vary widely within rupturing fault zones [*Bouchon*, 1997; *Olsen et al*., 1997]. For example, the shear stress drops ($^{\triangle}\tau$) were up to 3.5–11 MPa, 20 MPa, and 50 MPa during the 1999 Chi-Chi earthquake [*Ma et al*., 2000; *Kanamori and Brodsky*, 2004], the 2011 Tohoku earthquake [*Iinuma et al*., 2011; *Hasegawa et al*., 2012; *Yoshida et al*., 2012], and the 1989 Loma Prieta earthquake [*Bouchon*, 1997], respectively. Therefore, the coseismic mean principal stress drops before and after the three earthquakes ($^{\triangle}\sigma_m = (^{\triangle}\sigma_1 + {}^{\triangle}\sigma_2 + {}^{\triangle}\sigma_3)/3$) can be estimated to be about 3–9 MPa, 39 MPa, and 52 MPa, respectively, using $^{\triangle}\sigma_m = 2\cdot{}^{\triangle}\tau/[3\cdot\sin(2\theta)]$, which can be done if the effect of the intermediate principal stress is neglected (i.e., $^{\triangle}\sigma_2 = 0$) and we assume that the principal vertical stress is constant and provided by gravity for thrust faulting [*Scholz*, 2002; *Kanamori and Brodsky*, 2004; *Chen et al*., 2016]. Here the dips (θ) of the seismogenic faults are about 30°, 10°, and 70° for the Chi-Chi [*Yeh et al*., 2007], Tohoku [*Chester et al*., 2012], and Loma Prieta [*Dietz and Ellsworth*, 1990] earthquakes, respectively. This indicates that the coseismic mean principal stress drop ($^{\triangle}\sigma_m$) varies greatly over the fault for various earthquake events and may even exceed 50 MPa. Consequently, an appropriate β should be used to estimate the temperature change based on $^{\triangle}\sigma_m$.

For example, rock sample C01 was collected from the TCDP Hole-A, which locates at 120.73916°E, 24.20083° N [*Lin et al*., 2007]. The depth of this sample was at ~1105 m being very close to the principal slip zone of the fault at ~1111 m which ruptured during the 1999 Chi-Chi earthquake (Figure S2). The hypocenter was located at 120.75°E, 23.87°N, with a depth of 7 km [*Ma et al*., 2000]. The measurement results show that β of rock sample C01 (β_{C01}) is 4.25–4.29 mK/MPa when the confining pressure changes are within 30 MPa to 50 MPa, but will be up to 4.62–4.89 mK/MPa when the confining pressure changes reduce to less than 10 MPa (Figure 8f and Table S2). If we estimate the coseismic temperature decrease ($^{\triangle}T$) for the 1999 Chi-Chi earthquake, the β_{C01} value of 4.62–4.89 mK/MPa should be used but not 4.25–4.29 mK/MPa since $^{\triangle}\sigma_m$ was ~3–9 MPa. Using the data of β_{C01} and $^{\triangle}\sigma_m$, the coseismic temperature decrease ($^{\triangle}T$) can be estimated as ~14–44 mK. It is approximately close to the magnitude of the maximum negative temperature anomaly (~25 mK) measured in the TCDP Hole-A drilled into the Chelungpu Fault at ~6 years after the earthquake [*Kano et al*., 2006].

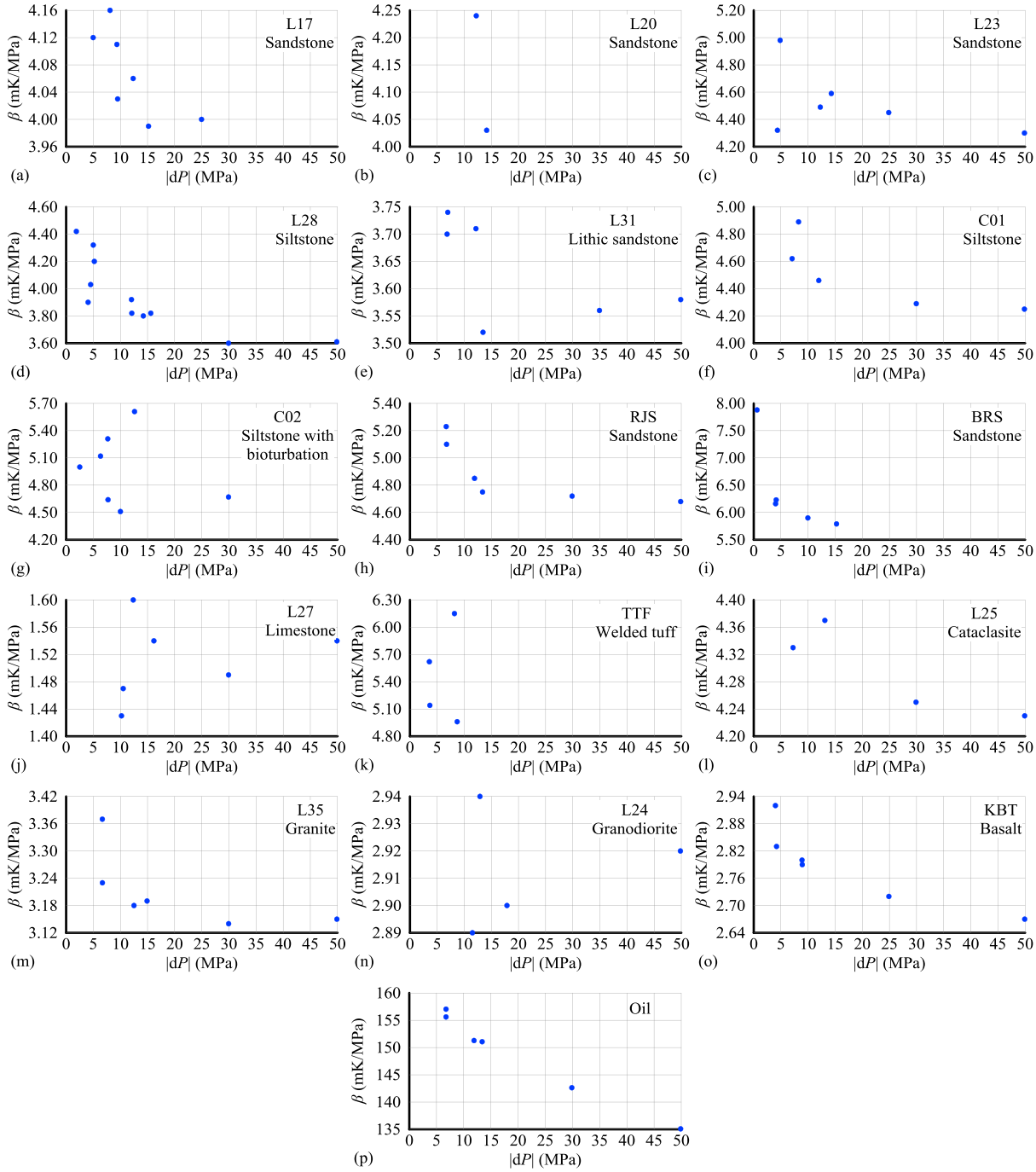

Figure 8. Measurements of β for each rock specimen and silicone oil at different pressure changes ($|dP|$ is the absolute value of confining pressure change) including both loading and unloading data.

In order to compare the temperature change estimated using our laboratory data with the negative temperature anomaly observed in the TCDP Hole-A by *Kano et al.* [2006], however, the following problems have to be solved. First, we need to obtain the stress drop around the depth of the fault observed in the TCDP Hole-A rather than the stress drop of ~3–9 MPa around the depth of earthquake hypocenter, and temperature profile diffused for ~6 years from the temperature profile immediately after the earthquake including the effect of stress drop. In addition, the temperature effects of pore water and pore pressure change should be considered. Usually, the porous rocks are saturated with ground water, especially in the deep. For the water-saturated rocks and dry rocks, there must be different temperature response

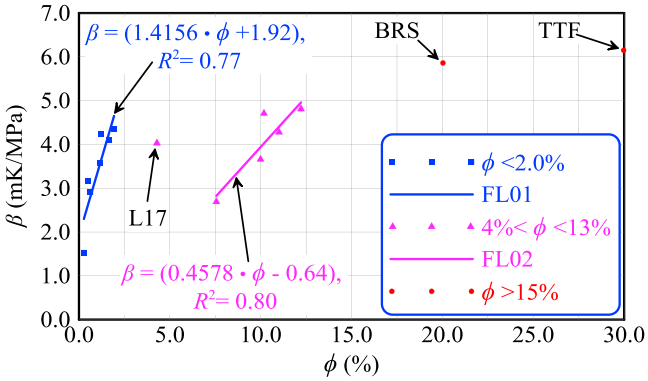

Figure 9. The relationship between β and porosity (ϕ) for all 15 dry rock samples. The blue squares, pink triangles, and red dots are the results when the porosity is within 2.0%, ranging from 4.0% to 13.0%, and more than 15.0%, respectively. The blue line (FL01) and pink line (FL02) are the linear fitting curves when the porosity is within 2.0% and ranging from 4.0% to 13.0%, respectively.

mechanisms to the coseismic stress change. Probably, the β of water-saturated rocks may be lower than that of dry rocks if the pore pressure keeps constant before and after earthquakes because the volumetric heat capacity (ρc) of water (~4.173 MJ/(m^3 K)) is much higher than the ρc of dry rocks (~1.261–2.352 MJ/(m^3 K)) (Tables 1 and 2). Nevertheless, the β of water is up to ~17.67 mK/MPa which is an order of magnitude higher than the β of dry rocks (1.5–6.2 mK/MPa) (Tables 1 and 2). Thus, the temperature of the pore water may vary largely even if the pore pressure change is small. In such case, the coseismic temperature decrease should be larger than that estimated using the β of dry rocks.

5.3. Effects of Porosity (ϕ) and Bulk Modulus (K) on β

The temperature response of sedimentary rocks to stress change (with a β of about 3.5 mK/MPa to 6.2 mK/MPa) is larger than that of igneous and metamorphic rocks (with a β that ranges from 2.5 mK/MPa to 3.2 mK/MPa) (Table 1). Furthermore, β fluctuates widely for different sandstones. Consequently, the effects of porosity (ϕ) and bulk modulus (K) on β require discussion.

5.3.1. Relationship Between β and Porosity (ϕ)

Figure 9 shows that β generally increases with porosity (ϕ) for all 15 rock samples. Additionally, there are two good correlations between β and porosity (ϕ) when porosity is within 2.0% and ranges from 4.0% to 13.0% (except for L17). The linear fitting lines FL01 and FL02 are expressed as equations (8) and (9), respectively. A relationship for situations where porosity is more than 15% cannot be found because we have only two measurement results from the Berea sandstone (BRS) and Tage welded tuff (TTF) (Figure 9).

$$\mathrm{FL01}: \beta = (1.4156 \cdot \phi + 1.92), R^2 = 0.77, \phi < 2.0\%, \tag{8}$$

$$\mathrm{FL02}: \beta = (0.4578 \cdot \phi - 0.64), R^2 = 0.80, 4.0\% < \phi < 13.0\%, \tag{9}$$

in which, R^2 is the coefficient of determination (similarly hereinafter), and the units of β and ϕ are mK/MPa and %, respectively.

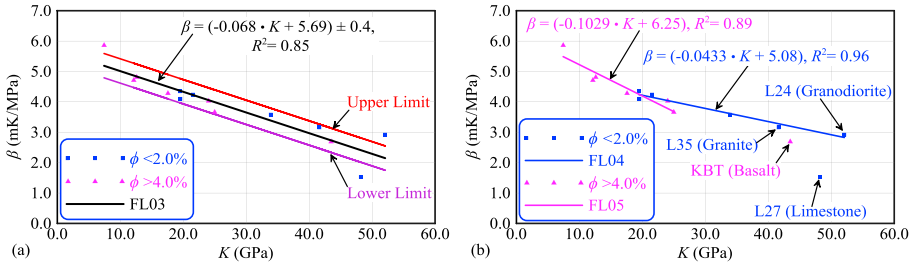

Figure 10. The relationships between β and K (a) for all rock samples except TTF and (b) in two groups divided according to porosity. The blue squares and pink triangles correspond to the results for rocks in which the porosity is less than 2.0% and more than 4.0%, respectively. The black line (FL03) is the linear fitting curve for the 14 rock samples (all except TTF). The red and purple lines are the upper and lower limits, respectively. The blue line (FL04) and pink line (FL05) are the linear fitting curves for porosities less than 2.0% (except for L27) and more than 4.0% (except for KBT), respectively.

5.3.2. Relationship Between β and Bulk Modulus (K)

The more interesting aspect of this work is that there may be a good linear correlation between the measurement results of β and the bulk modulus (K) (Figure 10a). This applies to 14 of the 15 rock samples; K for the Tage welded tuff (TTF) was lacking (Table 1):

$$\mathrm{FL03}: \beta = (-0.068{\cdot}K + 5.69) \pm 0.4, R^2 = 0.85, \tag{10}$$

where the units of β and K are mK/MPa and GPa, respectively (similarly hereafter).

If the results for β are divided into two groups based on porosity, we can obtain two improved linear correlations between β and K when porosities are less than 2.0%, with the exception of L27 Limestone (equation (11)), and more than 4.0%, with the exception of Karatsu basalt (KBT) (equation (12)) (Figure 10b).

$$\mathrm{FL04}: \beta = (-0.0433{\cdot}K + 5.08), R^2 = 0.96, \phi < 2.0\%, \tag{11}$$

$$\mathrm{FL05}: \beta = (-0.1029{\cdot}K + 6.25), R^2 = 0.89. \phi > 4.0\%. \tag{12}$$

These empirical equations (equations (10)–(12)) will be very useful for estimating the distribution of β in the crust, because K can be calculated by [*ASTM*, 1999]

$$K = \rho\left(3V_p^2 - 4V_s^2\right)/3, \tag{13}$$

when the profiles of crustal density (ρ) and velocities (V_p, V_s) have been obtained from gravity surveys and seismic exploration.

In Figure 10b, despite the porosity of L27 being less than 2.0%, β_{L27} deviates from fitting line FL04 and instead trends to FL05 because it is a chemically deposited limestone. Meanwhile, β_{KBT} deviates from fitting line FL05 and instead trends to FL04, even though the porosity of KBT is more than 4.0% (~7.56%). However, the Karatsu basalt (KBT) is a typical igneous unit, so its thermodynamic properties are close to those of the granite (L35) and granodiorite (L24). This implies that there will be different correlations between β and K for sedimentary, igneous, and metamorphic rocks. Unfortunately, it is difficult to obtain correlations for igneous and metamorphic because only two igneous rocks (L35 and KBT) and two metamorphic rocks (L24 and L25) were measured in this study.

6. Conclusions

Properties that affect the temperature response of rocks to changes in stress are critical for understanding temperature anomalies in the crust. Consequently, we have developed a new hydrostatic compression system to measure the adiabatic pressure derivative of the temperature (β) for rock samples. In this hydrostatic compression system, the rock specimen center can reach adiabatic conditions within the first several seconds (~10 s when the diameter and height of rock specimen are 5.0 cm each) following rapid loading/unloading. In this case, an accurate value for β can be calculated for the rock, based on observations of temperature step changes in the rock sample center during the loading/unloading process. Using this experimental system, we measured 15 dry rocks, including representative lithologies of sedimentary, igneous, and metamorphic rocks sampled from the Longmenshan Fault Zone, the Chelungpu Fault Zone (TCDP Hole-A), and several quarries worldwide. The measurements of β for most rocks were ~1.5 mK/MPa to 6.2 mK/MPa. All of these results can be confirmed by comparing the temperature changes in the rock sample center predicted by finite element modeling with those determined by experiments. The temperature response of sedimentary rocks to stress change (β ranges from 3.5 mK/MPa to 6.2 mK/MPa) is larger than that of igneous and metamorphic rocks (β ranges from 2.5 mK/MPa to 3.2 mK/MPa). For most rocks, β decreases as the change in confining pressure ($|\mathrm{d}P|$) increases. It is significant that there is good linear correlation between β and the porosity (ϕ) and bulk modulus (K). These empirical relationships are very useful for estimating the distribution of β in the crust, because K can be estimated when profiles of crustal density (ρ) and velocities (V_p, V_s) are obtained from gravity surveys and seismic exploration.

The new hydrostatic compression system and experimental method developed in this study are reliable and provide a convenient system for obtaining accurate β values for laboratory-based rock samples. In

actual geological settings, porous rocks are usually saturated with fluid (e.g., ground water, oil), which can influence β. Consequently, a very important aspect of future work will be to analyze the theory behind β for fluid-saturated rocks and carry out systematic experimental assessments of such geological units.

Acknowledgments

We thank Takehiro Hirose for providing the Karatsu basalt sample, Kentaro Hatakeda for partial technical support, and Xiaobin Shi, Hehua Xu, Shunyun Chen, Peixun Liu, Chi-Yuen Wang, Lucie Capova, Ziying Xu, and Zongxing Li for helpful discussions. Yuanzheng Lu and Xianrong Cen gave guidance to calculate the thermodynamic parameters of tap water by TEOS-2010. We really thank the reviewer for careful reading and constructive comments which help us to improve this manuscript. This work was supported by the National Natural Science Foundation of China (41474065, 41106086, 41330211, and 41376059), the Instrument Developing Project of the Chinese Academy of Sciences (YZ201136), the Strategic Priority Research Program of the Chinese Academy of Sciences (XDA11040303 and XDA13010104), and the CAS Scholarship. Weiren Lin acknowledges the supports of Japan Society for the Promotion of Science (JSPS KAKENHI Grant Numbers JP25287134 and JP16H04065). We have listed all the data in the supporting information of this paper.

References

ASTM (1999), ASTM standard test method for laboratory determination of pulse velocities and ultrasonic elastic constant of rock, American Society for Testing and Materials, Designation, D2845-95, 6.

Boley, B. A., and J. H. Weiner (1960), *Theory of Thermal Stresses*, Wiley, New York.

Bouchon, M. (1997), The state of stress on some faults of the San Andreas system as inferred from near-field strong motion data, *J. Geophys. Res.*, *102*(B6), 11,731–11,744, doi:10.1029/97JB00623.

Carreno, E., R. Capote, A. Yague, J. Tordesillas, M. Lopez, J. Ardizone, A. Suarez, A. Lzquierdo, M. Tsige, and J. Martinez (2001), *Observations of Thermal Anomaly Associated to Seismic Activity From Remote Sensing*, pp. 265–269, Gener. Assem. of Eur. Seismol. Com., Portugal.

Chen, S., L. Liu, P. Liu, J. Ma, and G. Chen (2009), Theoretical and experimental study on relationship between stress-strain and temperature variation, *Sci. China, Ser. D Earth Sci.*, *52*(11), 1825–1834.

Chen, S., P. Liu, L. Liu, and J. Ma (2013), A phenomenon of ground temperature change prior to Lushan earthquake observed in Kangding, *Seismolog. Geol.*, *35*(3), 634–640.

Chen, S., P. Liu, Y. Guo, L. Liu, and J. Ma (2015), An experiment on temperature variations in sandstone during biaxial loading, *Phys. Chem. Earth*, *85–86*, 3–8, doi:10.1016/j.pce.2014.10.006.

Chen, S., P. Liu, L. Liu, and J. Ma (2016), Bedrock temperature as a potential method for monitoring change in crustal stress: Theory, in situ measurement, and a case history, *J. Asian Earth Sci.*, *123*, 22–33, doi:10.1016/j.jseaes.2016.03.018.

Chester, F. M., J. J. Mori, S. Toczko, N. Eguchi, Y. Kido, S. Saito, Y. Sanada, L. Anderson, J. H. Behrmann, and S. Bose (2012), Integrated Ocean Drilling Program Expedition 343/343T preliminary report, Japan Trench Fast Drilling Project (JFAST), Integrated Ocean Drill. Project Prelim. Rep., 343, 1 April–24 May and 5–19 July.

Cooper, H., and G. Simmons (1977), The effect of cracks on the thermal expansion of rocks, *Earth Planet. Sci. Lett.*, *36*(3), 404–412.

Dietz, L. D., and W. L. Ellsworth (1990), The October 17, 1989, Loma Prieta, California, earthquake and its aftershocks: Geometry of the sequence from high-resolution locations, *Geophys. Res. Lett.*, *17*(9), 1417–1420, doi:10.1029/GL017i009p01417.

Franklin, J. (1979), Suggested methods for determining water content, porosity, density, absorption and related properties and swelling and slake-durability index properties, *Int. J. Rock Mech. Min. Sci.*, *16*(2), 143–151.

Fulton, P. M., et al. (2013), Low coseismic friction on the Tohoku-Oki fault determined from temperature measurements, *Science*, *342*(6163), 1214–1217, doi:10.1126/science.1243641.

Gustafsson, S. E. (1991), Transient plane source techniques for thermal conductivity and thermal diffusivity measurements of solid materials, *Rev. Sci. Instrum.*, *62*(3), 797–804, doi:10.1063/1.1142087.

Hasegawa, A., K. Yoshida, Y. Asano, T. Okada, T. Iinuma, and Y. Ito (2012), Change in stress field after the 2011 great Tohoku-Oki earthquake, *Earth Planet. Sci. Lett.*, *355*, 231–243.

Iinuma, T., M. Ohzono, Y. Ohta, and S. Miura (2011), Coseismic slip distribution of the 2011 off the Pacific coast of Tohoku earthquake (*M* 9.0) estimated based on GPS data—Was the asperity in Miyagi-oki ruptured?, *Earth Planets Space*, *63*(7), 643–648.

Inazu, D., Y. Ito, D. Saffer, and R. Hino (2014), An abrupt seafloor water-temperature increase in the epicentral region of the 2011 Tohoku earthquake, Japan Geoscience Union Meeting 2014.

ISO (2008), *Plastics-Determination of Thermal Conductivity and Thermal Diffusivity-Part 2: Transient Plane Heat Source (Hot Disc) Method, International Standard ISO 22007–2*, Int. Organ. for Stand., Geneva, Switzerland.

Kanamori, H., and E. E. Brodsky (2004), The physics of earthquakes, *Rep. Prog. Phys.*, *67*(8), 1429.

Kano, Y., J. Mori, R. Fujio, H. Ito, T. Yanagidani, S. Nakao, and K.-F. Ma (2006), Heat signature on the Chelungpu fault associated with the 1999 Chi-Chi, Taiwan earthquake, *Geophys. Res. Lett.*, *33*, L14306, doi:10.1029/2006GL026733.

Kuo, L.-W., S.-R. Song, L. Huang, E.-C. Yeh, and H.-F. Chen (2011), Temperature estimates of coseismic heating in clay-rich fault gouges, the Chelungpu fault zones, Taiwan, *Tectonophysics*, *502*(3), 315–327.

Li, H., H. Wang, Z. Xu, J. Si, J. Pei, T. Li, Y. Huang, S.-R. Song, L.-W. Kuo, and Z. Sun (2013), Characteristics of the fault-related rocks, fault zones and the principal slip zone in the Wenchuan Earthquake Fault Scientific Drilling Project Hole-1 (WFSD-1), *Tectonophysics*, *584*, 23–42.

Li, H., et al. (2015), Long-term temperature records following the M_w 7.9 Wenchuan (China) earthquake are consistent with low friction, *Geology*, *43*(2), 163–166, doi:10.1130/g35515.1.

Lide, D. R. (2010), *CRC Handbook of Chemistry and Physics, 90th Edition (CD-ROM Version 2010)*, CRC press/Taylor and Francis, Boca Raton, Fla.

Lin, A., S. Wang, J. Hung, M. Wu, and C. Liu (2007), Lithostratigraphy of the Taiwan Chelungpu-Fault Drilling Project—A borehole and its neighboring region, central Taiwan, *Terr. Atmos. Oceanic Sci.*, *18*(2), 223.

Lin, W., E.-C. Yeh, J.-H. Hung, B. Haimson, and T. Hirono (2010), Localized rotation of principal stress around faults and fractures determined from borehole breakouts in hole B of the Taiwan Chelungpu-fault Drilling Project (TCDP), *Tectonophysics*, *482*(1), 82–91.

Lin, W., P. Fulton, R. Harris, O. Tadai, O. Matsubayashi, W. Tanikawa, and M. Kinoshita (2014), Thermal conductivities, thermal diffusivities, and volumetric heat capacities of core samples obtained from the Japan Trench Fast Drilling Project (JFAST), *Earth Planets Space*, *66*(1), 1–11, doi:10.1186/1880-5981-66-48.

Liu, D. (1981), Thermal properties of ceramics [in Chinese], *Heibei Ceramics*, *4*, 20–27.

Ma, J., and X. Shan (2000), An attempt to study fault activity using remote sensing technology—A case of the Mani earthquake, *Seismolog. Geol.*, 3000.

Ma, J., L. Liu, P. Liu, and S. Ma (2007), Thermal precursory pattern of fault unstable slip: An experimental study of en echelon faults, *Chin. J. Geophys.*, *50*(4), 995–1004.

Ma, J., S. I. Sherman, and Y. Guo (2012), Identification of meta-instable stress state based on experimental study of evolution of the temperature field during stick-slip instability on a 5° bending fault, *Sci. Chin. Earth Sci.*, *55*(6), 869–881, doi:10.1007/s11430-012-4423-2.

Ma, K. F., T. R. A. Song, S. J. Lee, and H. I. Wu (2000), Spatial slip distribution of the September 20, 1999, Chi-Chi, Taiwan, earthquake (M_w7. 6)—Inverted from teleseismic data, *Geophys. Res. Lett.*, *27*(20), 3417–3420, doi:10.1029/2000GL011393.

McTigue, D. (1986), Thermoelastic response of fluid-saturated porous rock, *J. Geophys. Res.*, *91*(B9), 9533–9542, doi:10.1029/JB091iB09p09533.

Milne, J. (1886) *Earthquakes and Other Earth Movements*, D. Appleton and Co., New York.

Mosenfelder, J. L., P. D. Asimow, and T. J. Ahrens (2007), Thermodynamic properties of Mg_2SiO_4 liquid at ultra-high pressures from shock measurements to 200 GPa on forsterite and wadsleyite, *J. Geophys. Res.*, *112*, B06208, doi:10.1029/2006JB004364.

Olsen, K. B., R. Madariaga, and R. J. Archuleta (1997), Three-dimensional dynamic simulation of the 1992 Landers earthquake, *Science*, *278*(5339), 834–838, doi:10.1126/science.278.5339.834.

Orihara, Y., M. Kamogawa, and T. Nagao (2014), Preseismic changes of the level and temperature of confined groundwater related to the 2011 Tohoku earthquake, *Sci. Rep.*, *4*, 6907, doi:10.1038/srep06907.

Ouzounov, D., and F. Freund (2004), Mid-infrared emission prior to strong earthquakes analyzed by remote sensing data, *Adv. Space Res.*, *33*(3), 268–273.

Qin, Y., X. Yang, B. Wu, Z. Sun, and X. Shi (2013), High resolution temperature measurement technique for measuring marine heat flow, *Sci. Chin. Technol. Sci.*, *56*(7), 1773–1778, doi:10.1007/s11431-013-5239-9.

Richter, D., and G. Simmons (1974), Thermal expansion behavior of igneous rocks, *Int. J. Rock Mech. Min. Sci. Geomech. Abstr.*, *11*, 403–411.

Scholz, C. H. (2002), *The Mechanics of Earthquakes and Faulting*, Cambridge Univ. Press, Cambridge.

Stixrude, L., and C. Lithgow-Bertelloni (2005), Thermodynamics of mantle minerals—I. Physical properties, *Geophys. J. Int.*, *162*(2), 610–632, doi:10.1111/j.1365-246X.2005.02642.x.

Tanaka, H., W. Chen, C. Wang, K. Ma, N. Urata, J. Mori, and M. Ando (2006), Frictional heat from faulting of the 1999 Chi-Chi, Taiwan earthquake, *Geophys. Res. Lett.*, *33*, L16316, doi:10.1029/2006GL026673.

Tanaka, H., W. Chen, K. Kawabata, and N. Urata (2007), Thermal properties across the Chelungpu fault zone and evaluations of positive thermal anomaly on the slip zones: Are these residuals of heat from faulting?, *Geophys. Res. Lett.*, *34*, L01309, doi:10.1029/2006GL028153.

Tronin, A. A., M. Hayakawa, and O. A. Molchanov (2002), Thermal IR satellite data application for earthquake research in Japan and China, *J. Geodyn.*, *33*(4), 519–534.

Waldbaum, D. R. (1971), Temperature changes associated with adiabatic decompression in geological processes, *Nature*, *232*(5312), 545–547.

Wang, C., M. Manga, C. Wang, and C. Chin (2012), Transient change in groundwater temperature after earthquakes, *Geology*, *40*, 119–122.

Wang, C. Y., L. P. Wang, M. Manga, C. H. Wang, and C. H. Chen (2013), Basin-scale transport of heat and fluid induced by earthquakes, *Geophys. Res. Lett.*, *40*, 3893–3897, doi:10.1002/grl.50738.

Wang, H., H. Li, J. Si, Z. Sun, and Y. Huang (2014), Internal structure of the Wenchuan earthquake fault zone, revealed by surface outcrop and WFSD-1 drilling core investigation, *Tectonophysics*, *619–620*, 101–114, doi:10.1016/j.tecto.2013.08.029.

Wang, L., and C. Zhu (1984), Anomalous variations of ground temperature before the Tangsan and Haiheng earthquakes, *J. Seismol. Res*, *7*(6), 649–656.

Wong, A. K., R. Jones, and J. G. Sparrow (1987), Thermoelastic constant or thermoelastic parameter?, *J. Phys. Chem. Solids*, *48*(8), 749–753.

Wong, A. K., J. G. Sparrow, and S. A. Dunn (1988), On the revised theory of the thermoelastic effect, *J. Phys. Chem. Solids*, *49*(4), 395–400, doi:10.1016/0022-3697(88)90099-6.

Wong, T.-F., and W. Brace (1979), Thermal expansion of rocks: Some measurements at high pressure, *Tectonophysics*, *57*(2), 95–117.

Yeh, E.-C., H. Sone, T. Nakaya, K.-H. Ian, S.-R. Song, J.-H. Hung, W. Lin, T. Hirono, C.-Y. Wang, and K.-F. Ma (2007), Core description and characteristics of fault zones from Hole-A of the Taiwan Chelungpu-Fault Drilling Project, *Terr. Atmos. Oceanic Sci.*, *18*(2), 327–357.

Yoshida, K., A. Hasegawa, T. Okada, T. Iinuma, Y. Ito, and Y. Asano (2012), Stress before and after the 2011 great Tohoku-oki earthquake and induced earthquakes in inland areas of eastern Japan, *Geophys. Res. Lett.*, *39*, L03302, doi:10.1029/2011GL049729.